Current-Voltage Analysis of Dual-Band *n-p-n* HgCdTe Detectors

David R. Rhiger[1] · James W. Bangs[1]

Abstract

We report an analysis of the current-voltage characteristics of a dual-band HgCdTe infrared detector built in an *n-p-n* configuration and designed for sequential mode operation in mid-wavelength (MW) and long-wavelength (LW) bands. The model treats the device as a pair of back-to-back *p-n* junctions and addresses both dark and illuminated conditions over a range of temperatures. We show that the assumption of ideal diode behavior (diffusion-only current) provides a very good first approximation, particularly at small bias voltages. We also find that a plot of the resistance-area product *RA* is the most sensitive indicator of the deviation from ideality, most of which is due to non-diffusion currents in the LW junction. We determine the apportionment of the applied voltage between the two junctions and show that for LW detection, less than half the total voltage appears across the reverse biased LW junction. Our approach should be useful in analyzing other dual-band test data and guiding design improvements.

Graphical Abstract
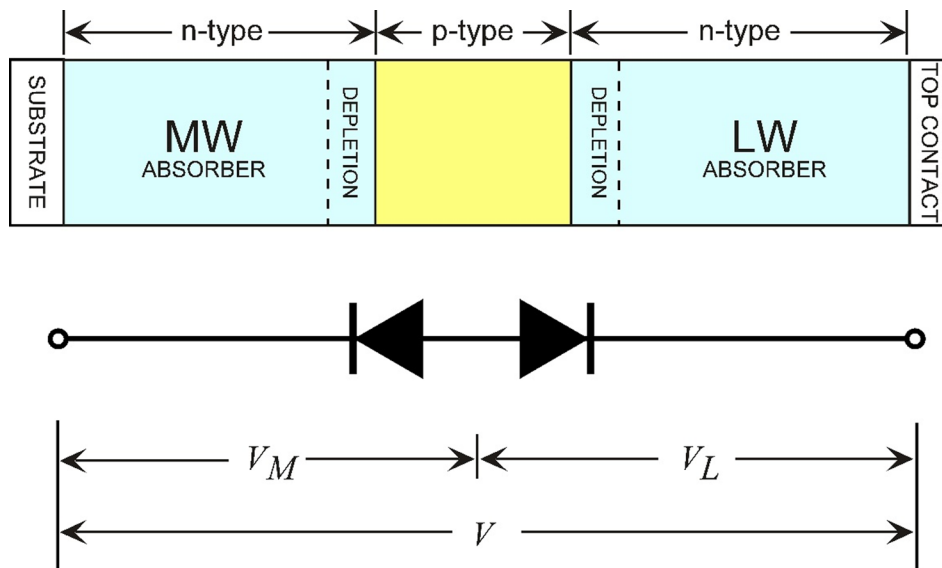
Introduction

In response to sensor system requirements, technological advances in the last several years have made it possible to fabricate focal planes that are sensitive in two wavelength bands of the infrared spectrum.[1–4] The most commonly used

✉ David R. Rhiger
  drhiger@raytheon.com

[1] Raytheon Vision Systems, Goleta, CA 93117, USA

material for dual-band detectors is HgCdTe.[5–12] The pair of bands selected for most applications are mid-wavelength (MW), which is nominally 3–5 μm, and long wavelength (LW), nominally 8–12 μm. Infrared focal plane assemblies are typically fabricated with a HgCdTe detector array hybridized to a silicon readout integrated circuit chip by means of one interconnect per pixel. Each pixel is sensitive in both bands, from which the signals are read alternately by switching the polarity of the applied bias voltage. This mode is known as sequential. The simultaneous mode, in contrast, requires two interconnects per pixel with precise control of etching to contact the center layer, and is more difficult to implement in small pitch focal planes. In this paper we study a sequential dual-band HgCdTe device consisting of two *n*-type absorber regions, with band gaps tailored to the MW and LW bands, respectively. The absorbers are separated by a *p*-type region, making an *n-p-n* configuration with two back-to-back *p-n* junctions.

It is desirable to understand the current-voltage relationships in this detector for purposes of analyzing test results and guiding future design improvements. A key constraint is that this is a two-terminal device, with no separate contact to the middle *p*-region. Another significant feature is the asymmetry between the MW and LW junctions, specifically the disparity in impedances. The interplay between the two junctions turns out to be critical to the analysis. To model the current-voltage relationship, early work was done by DeWames et al.[13–15] and by Rhiger and Bangs.[16] This paper is intended to expand upon those efforts. Various other approaches to modeling HgCdTe dual-band detectors,

some by finite-element numerical analysis, have been reported by several authors.[17–21] Also, in the literature one can find examples of the analysis of back-to-back Schottky barriers,[22–24] which are conceptually useful but do not apply directly because the physics of the junctions is different.

In this paper we develop a model for the current density-voltage (*J-V*) relationship of the full device and compare it with experimental results for a typical HgCdTe MW-LW detector. An important goal is to determine how the externally applied bias voltage is apportioned between the two junctions, as a function of the bias and the photon flux. Another goal is to extract from the test data an approximate current density-voltage characteristic for each junction. In addition, we identify the conditions under which the device conforms to ideal diode characteristics (defined by diffusion-only current) and where it shows evidence of additional dark current mechanisms. We find the resistance-area product *RA* at small positive bias to be particularly useful for comparing model and experiment.

Device Structure and Characteristics

The dual-band *n-p-n* device structure is represented in Fig. 1. The HgCdTe has been grown by molecular beam epitaxy (MBE). There are two *p-n* junctions, aligned in opposite directions. The incident IR flux enters through the CdZnTe substrate. The other components are the MW absorber, the highly doped *p*-type region, and the LW absorber. Both absorbers are *n*-type with a lower doping[10]
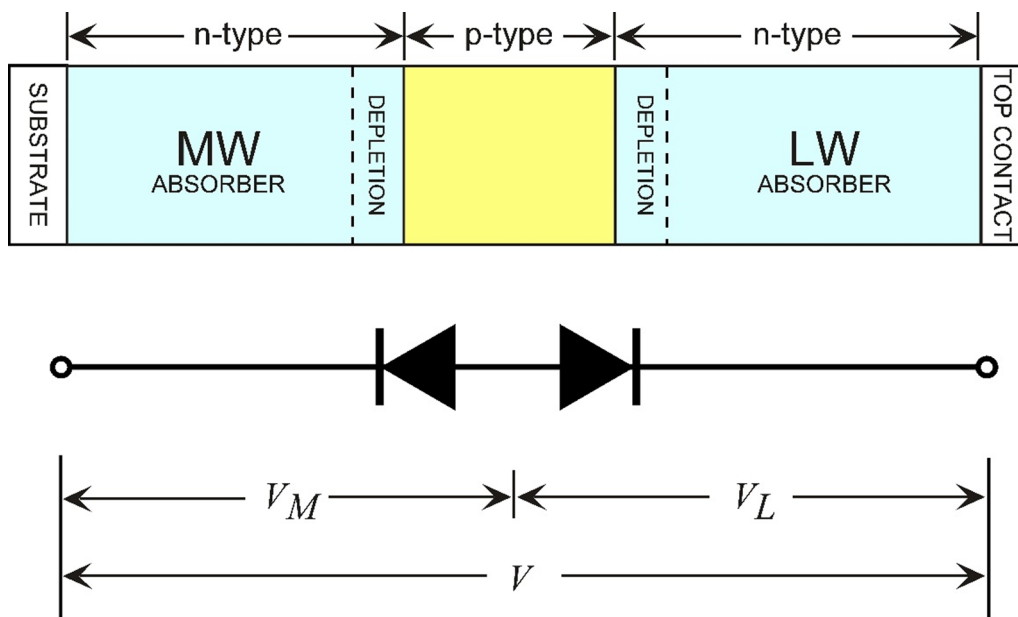

Fig. 1 Structure of the HgCdTe dual-band detector with two absorbers and their corresponding *p-n* junctions aligned back-to-back. Photons enter through the substrate on the left. Not having a separate contact to the *p*-region, this is a two-terminal device.

(about 3×10^{15} cm^{-3}) than the *p*-region ($> 1 \times 10^{17}$ cm^{-3}), causing most of the two depletion widths to reside within the absorbers. The bias voltage is applied to the metal contact at the top of the LW absorber. Potential differences across the MW and LW junctions are V_M and V_L, respectively. A series resistance is also present, but by curve-fitting of single-absorber LW HgCdTe devices[25] it has been found that the voltage across this resistance is small relative to that across the junction. An exception occurs when temperature is well above the normal operating range, causing dark current to be very large, a condition that we do not address. Therefore, to a good approximation the potential differences appear only across the depletion regions even when current is flowing. The total voltage on the device is

$$V \;=\; V_M + V_L \tag{1}$$

Individual pixels are formed into mesas by etching down past the depletion region of the MW junction. Since both junctions are in the same mesa and not far apart, they have the same area, so current density is the same in both. (In a case with unequal junction areas, current density can be replaced by current in much of the following discussion.) Formally, the device appears to be symmetric, but electrically it is notably asymmetric because, under most conditions, the direct-current impedance of the LW junction is much smaller than that of the MW junction. Also, because this is a two-terminal device with no direct access to the *p*-region, one cannot directly measure the electrical characteristics of either junction alone.

The *n-p-n* structure resembles a bipolar heterojunction transistor with a floating base, but it is designed to avoid transistor action.[6,10] The wide band gap of the base (*p*-region) forms a barrier to electron injection if either junction is forward biased. Also, its high doping promotes rapid recombination of excess electrons, inhibiting minority carrier (electron) transport in the base so that no current gain is possible.

Detector arrays and test chips were fabricated on MBE-grown HgCdTe/CdZnTe wafers. The test chips, containing several mini-arrays, were indium-bump hybridized to fanouts that provide direct electrical access to individual pixels. They were tested by standard techniques. Figure 2 shows the normalized spectral response curves per photon at 78 K from the sample we have selected for detailed analysis (no. 681534-C8). This is a member of a mini-array with a pixel area of 1.6×10^{-5} cm^2. MW and LW responses were measured at the respective biases of -50 mV and $+150$ mV. The cutoffs, defined at the level of 50% response, are 5.76 µm and 10.46 µm. Figure 3 displays the dark (zero field of view) current density-voltage
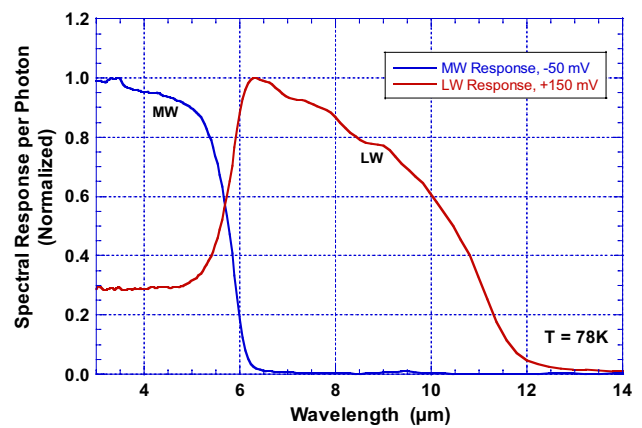

Fig. 2 Normalized spectral response per photon of the dual-band detector. MWIR response is obtained with -50 mV on the device and LWIR with $+150$ mV. Sample no. 681534-C8.
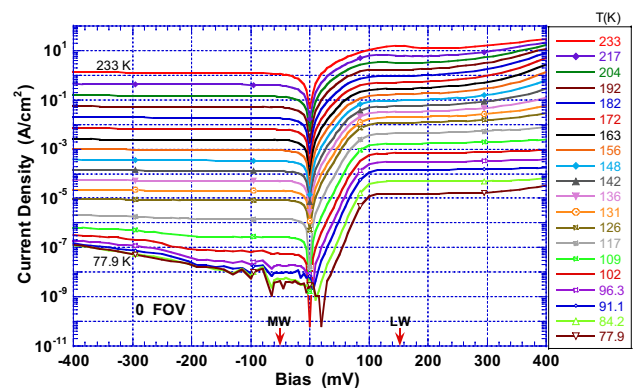

Fig. 3 Absolute value of the measured current density versus bias voltage at multiple temperatures, in dark (FOV = 0) conditions. Arrows mark the bias values for normal MWIR and LWIR detection. Same sample as Fig. 2.

(*J-V*) relation of the same sample at temperatures from 77.9 K to 233 K. Arrows mark the respective bias values for normal operation. At these two biases the curves are flat at most temperatures, suggesting diffusion-dominated current mechanisms when each junction is in small reverse bias. The dynamic resistance-area product $RA = dV/dJ$ is shown in Fig. 4 for the same device in the same temperature range. A local minimum in RA occurs near $+100$ mV, of which the parameters are addressed below in the model.

An initial test for ideal diode behavior, using the curves in Fig. 3, can be made on the narrow voltage interval between $+20$ mV and $+80$ mV where the MW junction is in small forward bias. It dominates in this region because of its much greater impedance. We fitted the curves to the generalized Shockley diode equation $J = J_0[\exp(qV/nkT) - 1]$ where *n* is the ideality factor,[26] temperature is T, Boltzmann's constant is k, and the unit charge is q. Figure 5
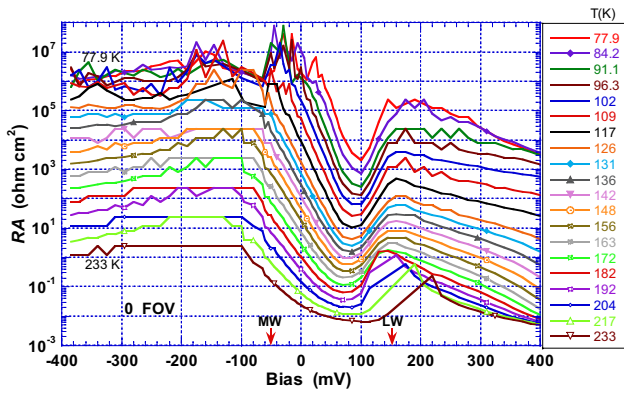
Fig. 4 Dynamic resistance area product *dV/dJ* obtained from the curves in Fig. 3.
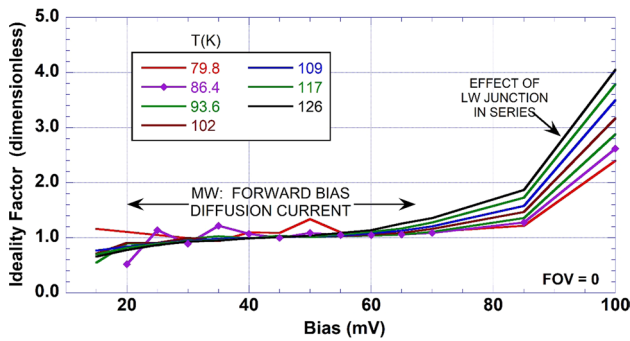

Fig. 5 Ideality factor of the MW junction in small forward bias, obtained from the curves in Fig. 3. The value at 1.0 indicates diffusion limited dark current within this voltage interval.

Fig. 6 Absolute value of the measured current density versus bias at 93.6 K, in the dark and under *f*/2 300 K BB illumination. The cusp is where the current changes sign.

Fig. 7 Absolute value of current density versus bias under *f*/2 300 K BB illumination at multiple temperatures. Curves are bunched together where photocurrent exceeds dark current, but spread out at higher temperatures. Same sample as Fig. 2.

shows that the fit gives $n = 1.0$, indicative of ideal (diffusion-limited) behavior in the MW junction. The relation is not applicable beyond $+80$ mV where the other junction begins to have influence. The range of ideality is explored further in the following discussions.

A comparison of dark and illuminated *J–V* curves is shown in Fig. 6. In the upper curve, the detector at 93.6 K is looking at a 300 K blackbody (BB) through an *f*/2 field of view (FOV). We observe competing photovoltaic effects. The LW photocurrent is higher than MW because there are more photons in that part of the spectrum. However, the point of zero current (the downward spike in the absolute value) is displaced, from zero volts in the dark to positive bias when illuminated, because of the greater open-circuit voltage produced by the wider band gap of the MW absorber. The full set of *J–V* curves under *f*/2 300 K BB illumination is shown in Fig. 7. Curves are bunched together at the lower temperatures where the photocurrent dominates and spread out at higher temperatures where the dark current exceeds photocurrent. The plots of *RA* when illuminated resemble those in Fig. 4 but with lower values.
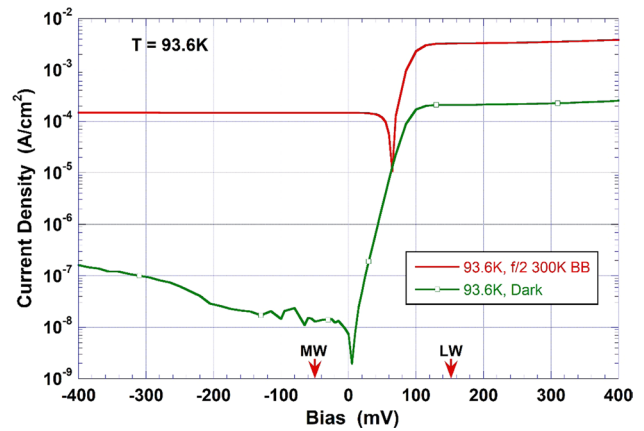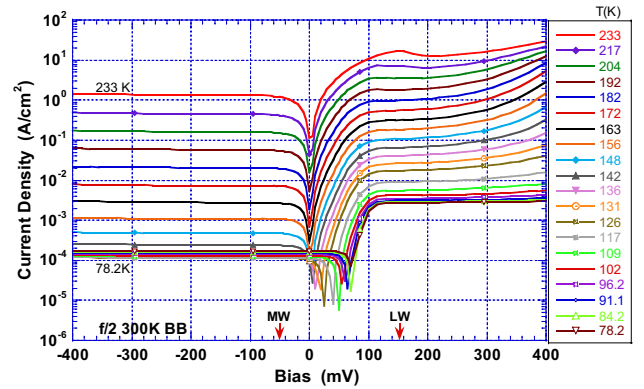
Dual-Band Device Model

The model begins with the assumption of ideal diode behavior[26] implying that currents arise only by diffusion from the quasi-neutral regions. In dark conditions, the respective equations for the MW and LW junctions are

$$J = J_{0M}\left(\exp\frac{qV_M}{kT} - 1\right) \tag{2}$$

$$J = -J_{0L}\left(\exp\frac{-qV_L}{kT} - 1\right) \tag{3}$$

The current density J is the same for both. The ideality factor is assumed to be unity and omitted. The reverse saturation current densities are J_{0M} and J_{0L} for the MW and LW junctions, respectively. The negative signs on J_{0L}

and on the bias of the LW junction are due to its reverse orientation. Under illumination the MW and LW absorbers will produce photocurrent densities J_{PM} and J_{PL}, respectively, which enter the equations with a sign opposite to the saturation current density.

$$J = J_{0M}(\exp \frac{qV_M}{kT} - 1) - J_{PM} \tag{4}$$

$$J = -J_{0L}(\exp \frac{-qV_L}{kT} - 1) + J_{PL} \tag{5}$$

Note that the four current densities J_{0M}, J_{0L}, J_{PM}, J_{PL} are treated as positive quantities and the equations take care of the signs. For any given condition of temperature, photon flux, and device characteristics, these currents assume fixed values. Combining Eqs. 4 and 5 with 1, the full *J–V* curve of the device becomes

$$V = \frac{kT}{q} \ln \left[\frac{(J_{PM} + J_{0M} + J)J_{0L}}{(J_{PL} + J_{0L} - J)J_{0M}} \right] \tag{6}$$

A closed form solution exists for *V* as a function of *J* but not for the inverse. The graph of *J* versus *V* will have a sigmoidal shape, as we show below. Also, the point of zero current, known as the open-circuit voltage, is

$$V_{J=0} = \frac{kT}{q} \ln \left[\left(\frac{J_{PM}}{J_{0M}} + 1 \right) \Big/ \left(\frac{J_{PL}}{J_{0L}} + 1 \right) \right] \tag{7}$$

The dynamic *RA* at any bias is found by differentiating Eq. 6 with respect to voltage and solving for dJ/dV.

$$\frac{1}{RA} = \frac{dJ}{dV} = \frac{(q/kT)\left[-J^2 + \left(J_{PL} + J_{0L} - J_{PM} - J_{0M} \right)J + \left(J_{PL} + J_{0L} \right)\left(J_{PM} + J_{0M} \right) \right]}{J_{PL} + J_{0L} + J_{PM} + J_{0M}} \tag{8}$$

One can show that there are two limiting cases of this equation. First, if $J = J_{PL} + J_{0L}$ then $dJ/dV = 0$, corresponding to a flat region of the *J-V* curve (at positive voltage) where the LW junction is in strong reverse bias. Similarly, if $J = -(J_{PM} + J_{0M})$, then again $dJ/dV = 0$, for a flat region (at negative voltage) with the MW junction in strong reverse bias. The same result is evident from Eq. 6 when *J* asymptotically approaches $(J_{PL} + J_{0L})$ or $-(J_{PM} + J_{0M})$, causing *V* to become large and positive, or large and negative, respectively. Therefore, under the assumption of ideal diode behavior, the graph of *J* versus *V* will have a sigmoidal shape with upper and lower bounds of $(J_{PL} + J_{0L})$ and $-(J_{PM} + J_{0M})$.

The local minimum of *RA*, as seen in Fig. 4, is a maximum of 1/*RA*, so we use Eq. 8 and set $d^2J/dV^2 = 0$. Consequently, the minimum is characterized by

$$(RA)_{\min} = \frac{4kT}{q} \frac{1}{J_{PL} + J_{0L} + J_{PM} + J_{0M}} \tag{9}$$

$$J_{\min RA} = \frac{1}{2}(J_{PL} + J_{0L} - J_{PM} - J_{0M}) \tag{10}$$

Additionally, the bias at the minimum turns out to be independent of the photocurrent.

$$V_{\min RA} = \frac{kT}{q} \ln \frac{J_{0L}}{J_{0M}} \tag{11}$$

Application to the Selected Sample

We apply the model to the detector represented in Figs. 2, 3, 4, 5, 6, and 7. To find values for the reverse saturation current densities J_{0M} and J_{0L} we refer to the measured dark current densities in Fig. 3. A good approximation over the full range of temperatures is obtained from the values at -60 mV and $+115$ mV, respectively, where each junction is in small reverse bias. In Fig. 8 we draw Arrhenius plots of the dark current density at these biases divided by T^3 versus reciprocal temperature, since diffusion current varies as $J_{diff} \propto n_i^2 \propto T^3 \exp\left(-E_g/kT\right)$ where n_i is the intrinsic carrier concentration and E_g is the band gap energy.[27] Except at the lowest temperatures, there are good straight-line fits to the data. Then, to get J_{0M} or J_{0L} at any temperature, we use the straight-line fits of Fig. 8
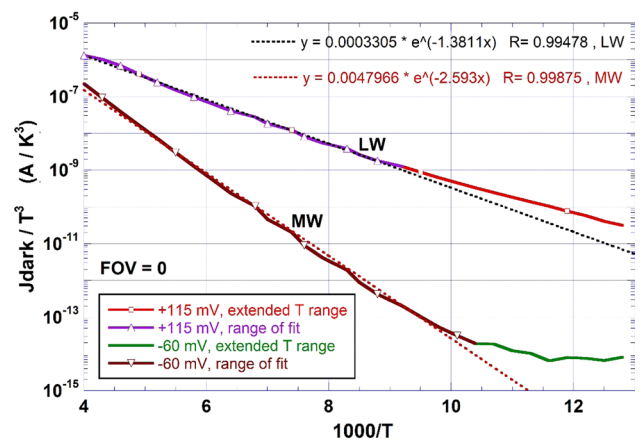

Fig. 8 Measured dark current densities divided by T^3, at two specified bias values, versus reciprocal temperature. The straight-line fits are used to define the reverse saturation currents of the LW and MW junctions.

and multiply by T^3. Moreover, the slopes correspond to cutoffs consistent with the spectral responses in Fig. 2. We also need the photocurrent densities, which can be obtained directly from the experimental curves. We find $J_{PM} = 1.67 \times 10^{-4}$ A/cm² and $J_{PL} = 3.47 \times 10^{-3}$ A/cm² under f/2 300 K BB illumination and assume them to be independent of bias and temperature to a good approximation. When $T > \approx 140$ K the dark currents become much larger, and the assumed photocurrents become unimportant. Thus, at high temperatures, the open-circuit voltage modeled by Eq. 7 shows no distinction between dark and illuminated conditions. In the following discussions we have selected $T = 102$ K as the temperature at which to explore several implications of the model.

Figure 9 shows the modeled direct current impedance (resistance) in the dark, for each junction versus the total applied bias. Values are obtained by first calculating J versus V with Eq. 6, and then inverting Eqs. 2 and 3 to determine V_M and V_L. Since the resistances are absolute and not differential, they are simply

$$R_M = V_M/JA \quad \text{and} \quad R_L = V_L/JA \quad (12)$$

where A is the junction area. At zero bias the impedance of the MW junction is four orders of magnitude larger, and it remains larger throughout most of the bias range, illustrating the electrical asymmetry of the dual-band detector.

Figure 10 is an example of the modeled sigmoid-shaped J–V curve at 102 K according to Eq. 6 under f/2 300 K BB FOV, compared with the measured data. Arrows mark the two operating biases. The fit is reasonable, but some deviations occur in positive bias due to non-diffusion components of the LW current.

In Fig. 11, the experimental values of RA for the device at 102 K, in both illuminated and dark conditions, are compared with the corresponding curves modeled according to the reciprocal of Eq. 8. Model and experiment agree
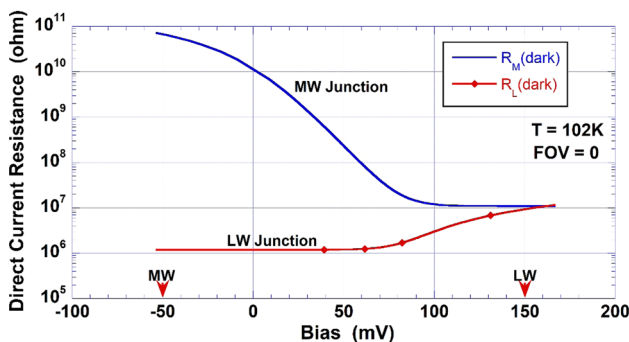
reasonably well between -50 mV and $+150$ mV. The agreement is especially good on the MW-dominated interval from -40 mV to $+80$ mV. This contains the interval in which we evaluated the ideality factor in Fig. 5. On the LW side of the minimum, the experimental curves are displaced to the right by about 20 mV, suggesting that even at small bias, the non-diffusion current mechanisms in the LW junction are not negligible. The plots of RA are apparently the most sensitive means of delineating the voltage interval in which the device conforms to ideal (diffusion-limited) behavior.

Figure 12 shows how the applied bias voltage is apportioned between the two junctions according to the model, under a variety of conditions at $T = 102$ K. To a very good approximation, the transitions in the electrostatic potential will be confined to the depletion regions. The position axis
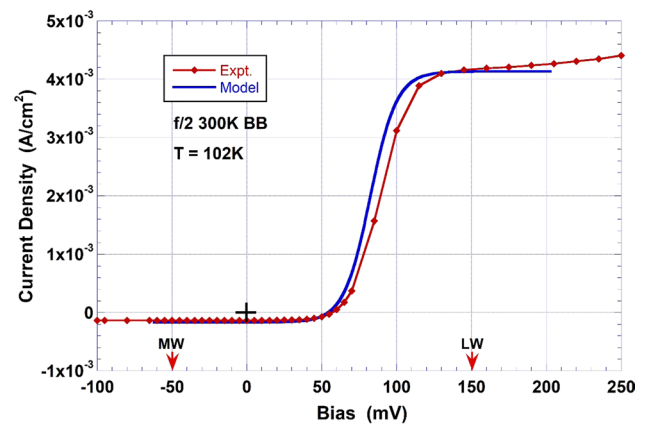

Fig. 10 Experimental and modeled current density at 102 K under f/2 300 K BB illumination. The model shows an ideal sigmoid shape, while measured values deviate at positive bias. The cross mark locates the origin.
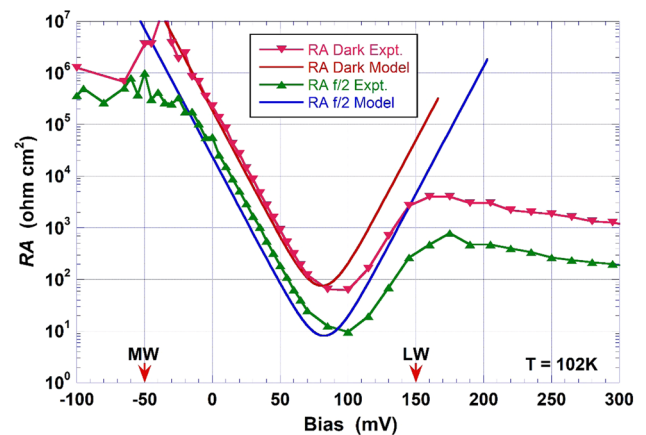

Fig. 9 Direct current (not differential) resistance of each junction versus total applied bias, in dark conditions according to the model. This illustrates the electrical asymmetry of the dual-band detector.

Fig. 11 Comparison of experiment and model for the dynamic resistance-area product at 102 K in the dark and under f/2 300 K BB illumination. This is the most sensitive indicator as to when the junctions conform to ideal diode (diffusion-limited) behavior.
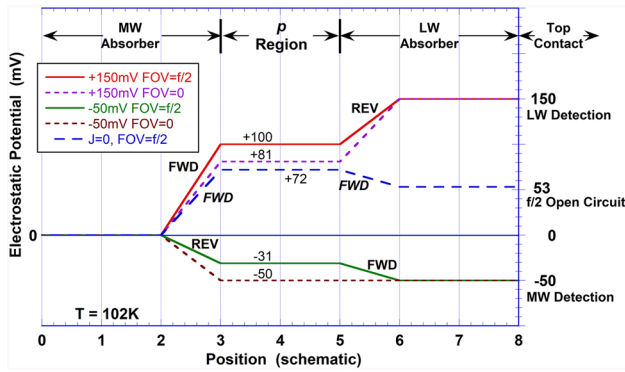
Fig. 12 Modeled electrostatic potential versus position through the device, for a variety of conditions, showing how the applied bias is apportioned between the two junctions. $T = 102$ K. States of forward and reverse bias are labeled.
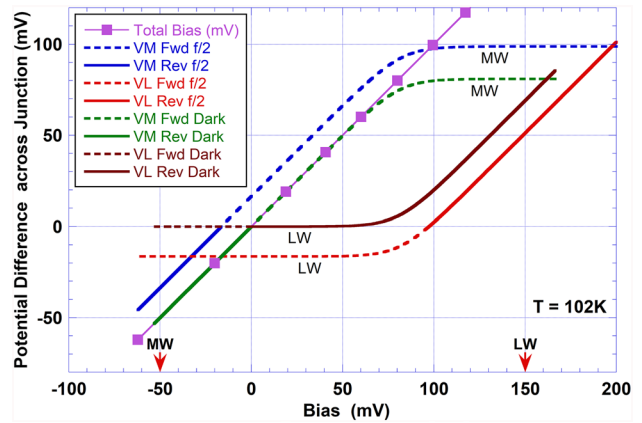

Fig. 13 Potential difference across each junction, as a function of total applied bias voltage, at 102 K. Inner and outer loops represent dark and *f*/2 300 K BB illumination, respectively. Curves are solid for reverse bias and dotted for forward.

is only schematic and does not reflect the physical size of the depletion widths under the different bias conditions. Also, we omit the curvature of the potential within the depletion regions. The solid lines represent the conditions for LW and MW detection under 300 K BB illumination with *f*/2 FOV. The dotted lines apply at the same two biases but with FOV = 0. Under illumination, at + 150 mV for LW detection, we find that 50 mV appears across the reverse-biased LW junction, and 100 mV is dropped across the forward-biased MW junction. In this case, only one third of the applied bias appears across the active junction. In the dark (or the limit of very low flux) for LW detection, the potential differences are $150 - 81 = 69$ mV, and 81 mV, across the active and forward-biased junctions, respectively, so that the active junction again sees less than half of the voltage. At the other operating bias, namely − 50 mV for MW detection when illuminated, there is 31 mV across the active reverse-biased MW junction and 19 mV across the forward-biased LW junction. In the dark, we find essentially all of the applied − 50 mV across the reverse-biased MW junction. Additionally, the dashed line represents the special case of zero current under illumination, where the open-circuit voltage is + 53 mV. Both junctions are forward biased. The MW photovoltaic effect is exactly balanced by the combination of the applied bias and the LW photovoltaic effect.

Figure 13 tracks the potential difference across each junction as a function of the total applied bias, in the dark and under *f*/2 300 K BB illumination, according to the model. The inner (green and brown) and outer (blue and red) loops apply to the dark and illuminated cases, respectively. Each loop sums to the total bias line in accord with Eq. 1. Both branches of the inner loop go through $(V, J) = (0, 0)$. Solid and dotted regions of each curve represent reverse bias, and forward bias, respectively. Under *f*/2, we find both junctions to be forward biased between − 16 mV and + 97 mV. However, at our standard operating biases (marked with arrows)
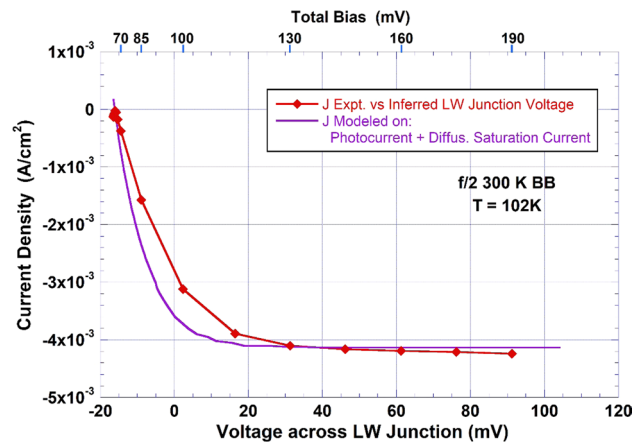
Fig. 14 Experimental *J–V* curve of the isolated LW junction under *f*/2 300 K BB illumination, as extracted from the test data, and the modeled curve for comparison.

under similar flux values, only one junction or the other will be forward biased. In the dark (or the limit of very low flux) no forward-bias overlap occurs.

The *J-V* curve of the isolated junction can be extracted by taking each experimental value of current density and matching it to the modeled *J-V* relation of the individual junction to find the single-junction voltage. Figure 14 is an example for the LW junction at 102 K in the *f*/2 300 K BB illumination. The lower horizontal axis is V_L. The upper horizontal axis shows the total bias *V*. The modeled curve, according to Eq. 5 is also shown. The difference is attributable to non-diffusion currents in the LW junction. The experimental open-circuit voltage of this junction is − 16 mV, which is near the calculated value of − 19 mV. The MW
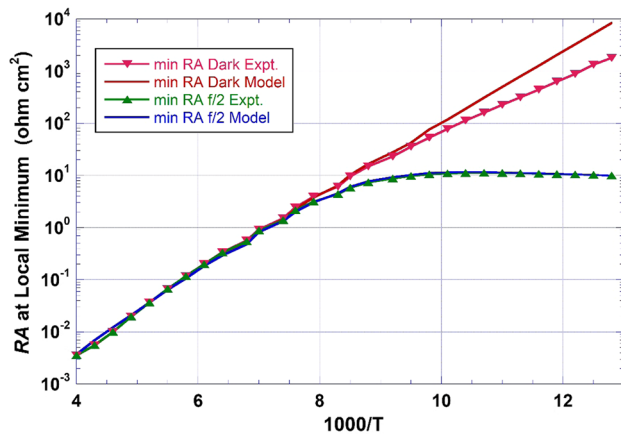
Fig. 15 Comparison of model and experiment for *RA* at the local minimum, versus temperature.

Fig. 16 Comparison of model and experiment for the bias at the local minimum of *RA*. The dark and *f*/2 cases agree very well, in accord with the model prediction of independence from photocurrent. Except at the highest temperatures, both differ from the modeled curve by about 10 mV or 15 mV due to non-diffusion currents, mostly in the LW junction.

junction curve can be obtained in the same manner and is closer to the model.

Characteristics at the local *RA* minimum, which appears in Fig. 4, can also be compared with the model. Figure 15 shows experimental values of $(RA)_{min}$ in both dark and *f*/2 300 K BB illumination at 102 K. They converge at higher temperatures ($1000/T < 7.5$) where dark current exceeds photocurrent, while the *f*/2 case levels off at lower T where photocurrent dominates. Solid lines show the model from Eq. 9. Agreement is very good, except for the dark case at the low temperatures where the added non-diffusion dark current brings *RA* slightly down. Another parameter of interest is the bias $V_{min\,RA}$ at which the minimum resides, as shown in Fig. 16. The dark and illuminated experimental values agree very well, consistent with the expected independence from photocurrent in Eq. 11, and compare well with the model given by the lower curve. For most of the range, the experiment and model run parallel about 10 mV or 15 mV apart, except at the highest temperatures.

Discussion

The back-to-back junction model assuming ideal *p–n* junctions provides a very good first approximation to the experimental device results. The current density-voltage curves show a sigmoid shape (Fig. 10) with upper and lower bounds defined by the sums of the respective reverse saturation current and photocurrent. The asymmetry of the structure is illustrated in terms of the direct current resistances of the two junctions modeled in Fig. 9. Deviations from the model, due to non-diffusion currents, are most sensitively revealed by a plot of *RA* versus bias (Fig. 11). We have used the model to determine how the applied bias is apportioned between the two junctions (Fig. 12). When biased for LW
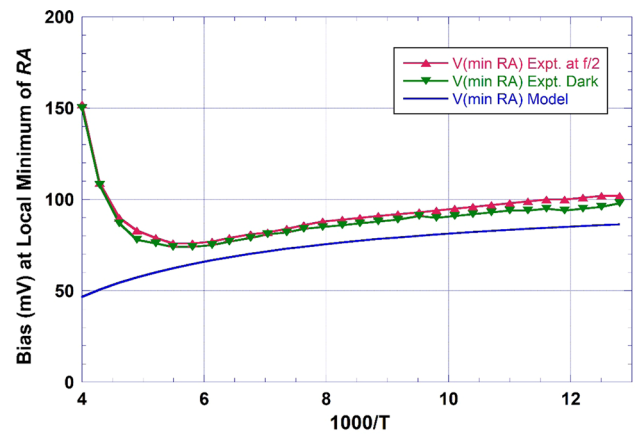
detection, whether illuminated or dark, less than half of the total applied bias voltage appears across the reverse biased LW junction, due to the strong interplay between junctions. Also, under illumination we find a voltage interval in which both junctions are forward biased, but this interval collapses to zero in the dark condition. In addition, given that it is not possible to test each junction independently, we have shown how to extract an approximate *J–V* characteristic for either junction.

Our investigation shows that for this device the selected bias voltages for normal operation, − 50 mV for MW and + 150 mV for LW, are well optimized. These voltages are far enough removed from zero, so that under *f*/2 300 K BB illumination, only the active junction will be reverse biased, but they do not put either junction too far into reverse bias, a condition that would likely increase the dark currents.

As noted above, the diffusion current in each junction that gives rise to ideal diode behavior originates by thermal generation within the quasi-neutral region (the absorber volume except for the depletion region). Nearly all of the photocurrent is also generated within the quasi-neutral region, and permits a simple, bias-independent addition to the junction current as implemented in Eqs. 4 or 5. For this reason, the ideal diode paradigm is applicable even in the presence of illumination. The model, however, does not account for excess (non-diffusion) dark currents. Instead, deviations from the model reveal their presence. Most of the excess current is associated with the LW junction, as in Figs. 10 and 11. Such currents are evident even at small bias (Fig. 16) where $V_{min\,RA}$ has been displaced toward more positive values than expected from the model. Probable mechanisms of excess dark current include trap-assisted tunneling, shunt

resistance paralleling the junction, and Shockley-Read-Hall generation within the depletion region.[25,28,29] However, constant energy tunneling of electrons from the valence band to the conduction band at the junction is not likely because the potential difference V_L is not large enough. Further work will be necessary to identify the non-diffusion dark currents in the dual-band detector.

Summary

We have investigated the current density-voltage characteristics of the dual-band MW–LW HgCdTe detector, built in the *n–p–n* configuration and designed for sequential mode operation. We have modeled the device in terms of a pair of back-to-back *p–n* junctions. The assumption of ideal diode (diffusion-limited) behavior provides a very good first approximation. The analysis reveals how the applied bias voltage is apportioned between the two junctions, which can assist in determining the optimum biases for operation of focal plane arrays. We find that for LW detection, less than half of the applied bias voltage appears across the reverse-biased active junction, and the rest is dropped across the forward-biased MW junction. We have shown how to extract an approximate *J–V* curve of the individual junction. A comparison of model and experiment, in several parameters, reveals the conditions in which non-diffusion dark currents contribute. The analysis has been performed in detail on one selected sample, but the methods are applicable to *n–p–n* detectors in general.

Conflict of interest The authors declare that they have no conflict of interest.

References

1. A. Rogalski, K. Adamiec, and J. Rutkowski, *Narrow-Gap Semiconductor Photodiodes* (Bellingham: SPIE Press, 2000), p. 280.
2. A. Rogalski, Toward third generation HgCdTe infrared detectors. *J. Alloys Compounds* 371, 53 (2004).
3. A. Rogalski, HgCdTe infrared detector material: history, status and outlook. *Rep. Prog. Phys.* 68, 2267–2336 (2005).
4. A. Rogalski, J. Antoszewski, and L. Faraone, Third-generation infrared photodetector arrays. *J. Appl. Phys.* 105, 091101 (2009).
5. J.M. Arias, M. Zandian, G.M. Williams, E.R. Blazejewski, R.E. DeWames, and J.G. Pasko, HgCdTe dual-band infrared photodiodes grown by molecular beam epitaxy. *J. Appl. Phys.* 70, 4620 (1991).
6. E.R. Blazejewski, J.M. Arias, G.M. Williams, W. McLevige, M. Zandian, and J. Pasko, Bias-switchable dual-band HgCdTe infrared photodetector. *J. Vac. Sci. Technol. B* 10, 1626 (1992).
7. R.D. Rajavel, D.M. Jamba, J.E. Jensen, O.K. Wu, C. Le Beau, J.A. Wilson, E. Patten, K. Kosai, J. Johnson, J. Rosbeck, P. Goetz, and S.M. Johnson, Molecular Beam Epitaxial Growth and Performance of Integrated Two-color HgCdTe Detectors Operating in the Mid-Wave Infrared Band. *J. Electron. Mater.* 26, 476 (1997).
8. R.D. Rajavel, D.M. Jamba, J.E. Jensen, O.K. Wu, J.A. Wilson, J.L. Johnson, E.A. Patten, K. Kosai, P. Goetz, and S.M. Johnson, Molecular beam epitaxial growth and performance of integrated multispectral HgCdTe photodiodes for the detection of mid-wave infrared radiation. *J. Cryst. Growth* 184, 1272 (1998).
9. E.P.G. Smith, L.T. Pham, G.M. Venzor, E.M. Norton, M.D. Newton, P.M. Goetz, V.K. Randall, A.M. Gallagher, G.K. Pierce, E.A. Patten, R.A. Coussa, K. Kosai, W.A. Radford, L.M. Giegerich, J.M. Edwards, S.M. Johnson, S.T. Baur, J.A. Roth, B. Nosho, T.J. De Lyon, J.E. Jensen, and R.E. Longshore, HgCdTe Focal Plane Arrays for Dual-Color Mid- and Long-Wavelength Infrared Detection. *J. Electron. Mater.* 33, 509 (2004).
10. R.A. Coussa, A.M. Gallagher, K. Kosai, L.T. Pham, G.K. Pierce, E.P. Smith, G.M. Venzor, T.J. de Lyon, J.E. Jensen, B.Z. Nosho, and J.R. Waterman, Spectral Crosstalk by Radiative Recombination in Sequential-Mode, Dual Mid-Wavelength Infrared Band HgCdTe Detectors. *J. Electron. Mater.* 33, 517 (2004).
11. E.P.G. Smith, A.M. Gallagher, T.J. Kostrzewa, M.L. Brest, R.W. Graham, C.L. Kuzen, E.T. Hughes, T. F. Mc Ewan, G.M. Venzor, E. A. Patten, and W.A. Radford, Large Format HgCdTe Focal Plane Arrays for Dual-Band Long-Wavelength Infrared Detection, *Proc. SPIE 7298*, 72981Y (2009).
12. E.P.G. Smith, G.M. Venzor, A.M. Gallagher, M. Reddy, J.M. Peterson, D.D. Lofgreen, and J.E. Randolph, Large-Format HgCdTe Dual-Band Long-Wavelength Infrared Focal-Plane Arrays. *J. Electron. Mater.* 40, 1630 (2011).
13. R.E. DeWames, C. Billman, K. Dang, A. Stoltz, and J. Pellegrino, Current versus Voltage Characteristics of HgCdTe Back-to-Back Photodiodes for the Detection of Infrared Radiation in the MWIR (3-5μm) and LWIR (8-10μm) Spectral Bands, *Proceedings of the Military Sensing Symposium Specialty Group on Detectors*, paper DF02 (2010).
14. R.E. DeWames, C. Billman, K. Dang, A. Stoltz, and J. Pellegrino, Resulting Current versus Voltage Characteristics of two HgCdTe Back to Back Photodiodes for the Detection of Infrared Radiation in the MWIR and LWIR Spectral Bands, *Extended Abstracts of the 2010 U.S. Workshop on the Physics and Chemistry of II-VI Materials* (2010), p. 83.
15. R.E. DeWames and J.G. Pellegrino, Modeling of the Measured Current vs. Voltage and Dynamic Impedance Area-Product of Back to Back HgCdTe MW/LW Heterostructure Photodiodes Built On CdZnTe and Composite Silicon Substrates, *Extended Abstracts of the 2012 U.S. Workshop on the Physics and Chemistry of II-VI Materials* (2012), p. 11.
16. D.R. Rhiger and J.W. Bangs, Current-Voltage Analysis of *n-p-n* HgCdTe Detectors, *Extended Abstracts of the 2012 U.S. Workshop on the Physics and Chemistry of II-VI Materials* (2012), p. 15.
17. K. Jozwikowski, and A. Rogalski, Computer modeling of dual-band HgCdTe photovoltaic detectors. *J. Appl. Phys.* 90, 1286 (2001).

18. E. Bellotti, and D. D'Orsogna, Numerical Analysis of HgCdTe Simultaneous Two-Color Photovoltaic Infrared Detectors. *IEEE J. Quant. Electron.* 42, 418 (2006).

19. M. Kopytko, W. Gawron, A. Kębłowski, D. Stępien, P. Martyniuk, and K. Jóźwikowski, Numerical analysis of HgCdTe dual-band infrared detector. *Opt. Quant. Electron.* 51, 62 (2019).

20. M. Vallone, M. Goano, A. Tibaldi, S. Hanna, D. Eich, A. Sieck, H. Figgemeier, G. Ghione, and F. Bertazzi, Challenges in multiphysics modeling of dual-band HgCdTe infrared detectors. *Appl. Optics* 59, 5656 (2020).

21. M. Vallone, M. Goano, A. Tibaldi, S. Hanna, A. Wegmann, D. Eich, H. Figgemeier, G. Ghione, and F. Bertazzi, Quantum Efficiency and Crosstalk in Subwavelength HgCdTe Dual Band Infrared Detectors. *IEEE J. Sel. Topics Quant. Electron.* 28, 3800309 (2022).

22. R. Nouchi, Extraction of the Schottky parameters in metal-semiconductor-metal diodes from a single current-voltage measurement. *J. Appl. Phys.* 116, 184505 (2014).

23. J. Osvald, Back-to-back connected asymmetric Schottky diodes with series resistance as a single diode. *Phys Stat. Sol. A* 212, 2754 (2015).

24. K. Tada, Parameter extraction from S-shaped current-voltage characteristics in organic photocell with opposed two-diode model: Effects of ideality factors and series resistance. *Phys. Stat. Sol. A* 212, 1731 (2015).

25. A.S. Gilmore, J. Bangs, and A. Gerrish, Current Voltage Modeling of Current Limiting Mechanisms in HgCdTe Focal Plane Array Photodetectors. *J. Electron. Mater.* 34, 913 (2005).

26. B.G. Streetman, *Solid State Electronic Devices*, second edition (Prentice-Hall, Englewood Cliffs, N.J., 1980), p. 152 and p. 179.

27. A.S. Grove, *Physics and Technology of Semiconductor Devices* (New York: John Wiley & Sons, 1967), p. 175.

28. A.S. Gilmore, J. Bangs, and A. Gerrish, VLWIR HgCdTe Detector Current-Voltage Analysis. *J. Electron. Mater.* 35, 1403 (2006).

29. M.A. Kinch, *State-of-the-Art Infrared Detector Technology* (Bellingham: SPIE Press, 2014), p. 11.